



**HAL**  
open science

# Optimal design of auxetic, additively manufactured, polymeric structures

Filippo Agnelli, Andrei Constantinescu, Grigor Nika

► **To cite this version:**

Filippo Agnelli, Andrei Constantinescu, Grigor Nika. Optimal design of auxetic, additively manufactured, polymeric structures. 2018. hal-01868830v1

**HAL Id: hal-01868830**

**<https://hal.science/hal-01868830v1>**

Preprint submitted on 5 Sep 2018 (v1), last revised 28 Nov 2023 (v2)

**HAL** is a multi-disciplinary open access archive for the deposit and dissemination of scientific research documents, whether they are published or not. The documents may come from teaching and research institutions in France or abroad, or from public or private research centers.

L'archive ouverte pluridisciplinaire **HAL**, est destinée au dépôt et à la diffusion de documents scientifiques de niveau recherche, publiés ou non, émanant des établissements d'enseignement et de recherche français ou étrangers, des laboratoires publics ou privés.

# OPTIMAL DESIGN OF AUXETIC, ADDITIVELY MANUFACTURED, POLYMERIC STRUCTURES

FILIPPO AGNELLI, ANDREI CONSTANTINESCU, AND GRIGOR NIKA

**ABSTRACT.** This work is concerned with the optimal design, additive manufacturing, and testing of microarchitected polymer materials with desired macroscopic mechanical properties. More precise, we are interested in designing and fabricating a materials microstructure in terms of the topology as well as material distribution of the individual phases within a periodic unit cell. In the design process we use the level set method to identify material regions and track boundary changes within the context of the smoothed interface. The combination of the level set method and the shape derivative obtained in the smoothed interface context allows us to capture, within the unit cell, the topological changes that take place. The obtained unit cells are smoothed and enhanced using standard image processing techniques and have periodically been multiplied into rectangular specimens. The specimens are manufactured using a commercial stereolithography Ember printer and mechanically tested. The observed fields are compared with predictions from the simulations.

## 1. INTRODUCTION

The ability to systematically design and additively manufacture multi-scale structures that exhibit globally desired mechanical properties is one the frontiers of modern material science. The advancement of 3D printing has enabled researchers to create high resolution structures with complex geometries at several scales. This in turn, enabled the creation of metamaterials that carry properties that are otherwise not possible to find in nature. Broadly speaking, metamaterials are assemblies of microstructures that derive their effective properties not just from the bulk composition but also from geometric arrangements of the structure. Hence, by producing different geometries at the microscopic scale and tiling them together, often in a periodic way, we can create macrostructures with desired properties. These different geometric arrangements make metamaterials possess unusual properties such as enhanced stiffness and energy absorption capabilities [15], [18], [24], indentation resistance, greater yield strength [23], crashworthiness [17], phononic performance [12] as well as many other interesting properties.

Since the seminal work of Lakes [20] to design auxetic structures, significant efforts have been devoted to the development of auxetic materials. Shape and topology optimization methods [1]–[4], [11], [35]–[36] arise as a natural way to design complex geometries. For periodic auxetic metamaterials the overall properties can be studied using homogenization theory where the effective coefficients computed take into account the bulk material composition as well as the geometry layout. Topology optimization using inverse homogenization exploits this fact in order to systematically identify optimal geometries for the unit cell. This in turn would produce a macrostructure with desired properties. The works of Wang, Mei,

---

*Date:* 2018/09/04.

*Key words and phrases.* additive manufacturing, topology optimization, 3D printing.

Wang [35], Michailidis [26], Nika & Constantinescu [29], Wang et.al. [37], among others, use inverse homogenization, the level set method and the Hadamard shape derivative to identify material regions and track boundary changes to systematically design auxetic shapes. Wang, Mei & Wang [35], Michailidis [26], design linear elastic and thermoelastic materials with negative Poisson’s ratio while Nika & Constantinescu [29] design linear elastic multimaterials with negative Poisson’s ratio.

The effective material tensor that characterizes the auxetic macrostructure a priori has orthotropic symmetry. Hence, the macrostructure, in 2D, is characterized by two Young moduli,  $E_1$ ,  $E_2$  and two Poisson ratios  $\nu_{12}$ ,  $\nu_{21}$ . The Poisson ratio  $\nu_{12}$  characterizes contraction of the structure in the direction of  $Oy$  axis when stretched in the direction of  $Ox$  axis and in general  $\nu_{12} \neq \nu_{21}$ . In literature, most auxetic metamaterials obtain their auxetic behavior through centers of rotations (see [19]). This type of materials tend to carry cubic symmetry, namely,  $\nu_{12} = \nu_{21}$ . Another interesting class of auxetic materials are re-entrant materials. For most re-entrant structures  $\nu_{12} \neq \nu_{21}$ . The most well known re-entrant auxetic structure is the inverted honeycomb structure first introduced by Almgren [8]. The inverted honey comb structure was also introduced as a “bi-mode” extremal material which supports a stress with a negative determinant in Milton & Cherkaev [27]. For isotropic structures it is well known that the Poisson ratio remains bounded in  $[-1, 0.5]$ . Since in general these are anisotropic materials, the bounds on Poisson’s ratio are wider  $(-\infty, +\infty)$  than in the isotropic case; indeed Poisson’s ratios smaller than negative one have been reported in Lakes [21]. In the topology optimization literature the auxetic shapes obtained tend to be exhibit cubic symmetry with the apparent Poisson’s ratio,  $\nu^* \in [-1, 0.5]$ . However, as was already mentioned, this need not be the case.

The aim of this paper is to complete a design cycle for several auxetic materials. The cycle consists of three steps (i) the design of the microarchitecture, (ii) the manufacturing of the material and (iii) the testing of the material. The goal is to obtain domain microarchitected materials with a prescribed elasticity tensor and apparent Poisson’s ratio. In order to reach this goal topology optimization will be used for the material design process. Materials will be manufactured using a desktop stereolithography 3D printer and then tested on standard tensile machine. Insight into the local mechanical fields is obtained using digital image correlation.

The paper is organized as follows. Section 2 presents the optimal design of the microarchitected material. It provides some basic results needed from the theory of homogenization, relate the effective coefficients to the apparent Poisson ratio, and sets up the optimization problem to systematically identify optimal auxetic shapes. Section 3 present the optimal auxetic microstructures obtained and describes some of their properties as well as the additive manufacturing process. Section 4 is dedicated to the experimental testing of the structures and the interpretation of results using digital image correlation. Additionally, an appendix reviews the approach used to measure the apparent Poisson’s ratio by DIC and the finite element method on periodic structures.

## 2. OPTIMAL DESIGN OF THE MICROARCHITECTURED MATERIAL

The link between the properties of the material at the scale of the microarchitecture and the macroscopic scale of the material is described using classical homogeneization theory. This defines a precise mathematical framework which enables the application of the topology

optimization algorithm to compute a microstructure such that the material has a prescribed elasticity tensor.

Next we shall only refer to the main results used in the sequel and recommend the classical literature on homogenization for details and proofs (see for example Sanchez-Palencia [32], Bakhvalov & Panasenko [9], Sanchez-Palencia, A. Zaoui [33], Allaire [1], Cioranescu & Donato [13], Mei & Vernescu [25] among others)

Let us consider a linear, elastic body occupying a bounded domain  $\Omega$  of  $\mathbb{R}^N$ ,  $N = 2, 3$ . Its periodic microstructure is of size  $\epsilon$  assumed to be small in comparison to the size of the domain and completely described by a rescaled unit cell  $Y = (-1/2, 1/2)^N \subset \mathbb{R}^N$ . The material properties in  $\Omega$  are represented by a periodic fourth order tensor  $\mathbb{A}(\mathbf{y})$  with  $\mathbf{y} = \mathbf{x}/\epsilon \in Y$  and  $\mathbf{x} \in \Omega$  the current points in the respective domains.

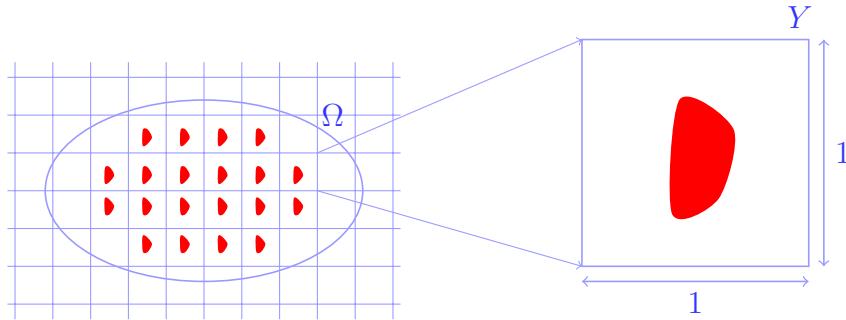


FIGURE 1. Schematic of the elastic periodic composite material.

The homogenized coefficients  $\mathbb{A}^H$  of the effective medium at the scale of  $\Omega$  are obtained from the following explicit computation on the unit cell  $Y$ :

$$A_{ijml}^H = \int_Y \mathbb{A}(E^{ij} + \varepsilon(\chi^{ij})) : (E^{m\ell} + \varepsilon(\chi^{m\ell})) d\mathbf{y} \quad (2.1)$$

where  $(\mathbf{e}_k)_{1 \leq k \leq N}$  is the canonical basis of  $\mathbb{R}^N$ .  $\mathbf{E}^{m\ell} = \frac{1}{2}(\mathbf{e}_m \otimes \mathbf{e}_\ell + \mathbf{e}_\ell \otimes \mathbf{e}_m)$  with  $m, \ell \in \{1, \dots, N\}$  denote a vector basis of the mean deformations applied on the unit cell.  $\chi^{m\ell}$  are the corresponding displacements fields created by these deformations on the unit cell  $Y$ . As such the displacement fields  $\chi^{m\ell}$  are solution of the following linear elastic problems with periodic boundary conditions:

$$-\operatorname{div} (\mathbb{A}(\mathbf{E}^{m\ell} + \varepsilon(\chi^{m\ell}))) = \mathbf{0} \text{ in } Y \quad (2.2)$$

where the displacement  $\chi^{m\ell}(\mathbf{y})$  is periodic in  $Y$  and has a zero average value on the unit cell

$$\langle \chi^{m\ell} \rangle_Y = \mathbf{0}.$$

The loading is given by the distributed body force  $-\operatorname{div} (\mathbb{A}(\mathbf{E}^{m\ell}))$ , which stems directly from the mean deformation field  $\mathbf{E}^{m\ell}$  and the distribution of elastic moduli  $\mathbb{A}$  in the unit-cell.

**Orthotropic elastic materials.** The homogenized tensor  $\mathbb{A}^H$  in (2.1) carries a natural orthotropic material symmetry. The linear elastic constitutive equation on the unit cell relating the mean stress and strain tensors, denoted as  $\boldsymbol{\sigma}^H$  and  $\boldsymbol{\varepsilon}^H$  respectively, has therefore the following expression for the two dimensional problems under consideration:

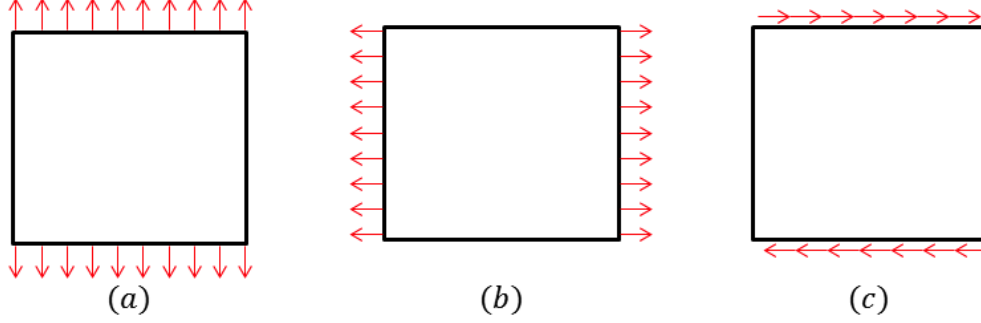


FIGURE 2. A schematic view of boundary displacements corresponding to the three mean deformation tensors  $\mathbf{E}^{m\ell}$  applied on a homogeneous unit cell  $Y$ : tensile deformations along the coordinate axes (a)  $\mathbf{E}^{11}$ , (b)  $\mathbf{E}^{22}$  and (c) the simple shear deformation  $\mathbf{E}^{12}$ .

$$\begin{pmatrix} \sigma_{11}^H \\ \sigma_{22}^H \\ \sigma_{12}^H \end{pmatrix} = \begin{pmatrix} A_{1111}^H & A_{1122}^H & 0 \\ A_{1122}^H & A_{2222}^H & 0 \\ 0 & 0 & 2A_{1212}^H \end{pmatrix} \begin{pmatrix} \varepsilon_{11}^H \\ \varepsilon_{22}^H \\ \varepsilon_{12}^H \end{pmatrix}$$

where  $\boldsymbol{\sigma}^H$  and  $\boldsymbol{\varepsilon}^H$  are the mean stress and strain respectively:

$$\boldsymbol{\sigma}^H = \langle \boldsymbol{\sigma} \rangle_Y \quad \boldsymbol{\varepsilon}^H = \langle \boldsymbol{\varepsilon} \rangle_Y.$$

Alternatively, one could express the effective strain as a function of the effective stress with the following effective material tensor:

$$\begin{pmatrix} \varepsilon_{11}^H \\ \varepsilon_{22}^H \\ \varepsilon_{12}^H \end{pmatrix} = \begin{pmatrix} 1/E_1 & -\nu_{12}/E_2 & 0 \\ -\nu_{21}/E_1 & 1/E_2 & 0 \\ 0 & 0 & 1/2G \end{pmatrix} \begin{pmatrix} \sigma_{11}^H \\ \sigma_{22}^H \\ \sigma_{12}^H \end{pmatrix}$$

where  $E_i$  and  $\nu_{ij}$  denote the homogenized Young moduli and Poisson's ratios respectively. In order to simplify the notation, we will drop the  $H$  superscript. Let us further remark, that by symmetry of the elastic compliance matrix, the following ratios have to be equal:

$$\frac{\nu_{12}}{E_2} = \frac{\nu_{21}}{E_1}$$

The elastic moduli,  $A_{ijkl}^H$ , can equally be expressed in terms of the compliance moduli, i.e. Young moduli and Poisson's ratios:  $A_{1111}^H = (1 - \nu_{12}\nu_{21})^{-1}E_1$ ,  $A_{2222}^H = (1 - \nu_{12}\nu_{21})^{-1}E_2$ ,  $A_{1122}^H = \nu_{21}(1 - \nu_{12}\nu_{21})^{-1}E_1$ ,  $A_{2211}^H = \nu_{12}(1 - \nu_{12}\nu_{21})^{-1}E_2$  with  $A_{1122}^H = A_{2211}^H$  as can be easily obtained from the inversion of the corresponding matrices.

A simple calculation immediately yields:

$$\nu_{12} = \frac{A_{1122}^H}{A_{2222}^H} \quad \text{and} \quad \nu_{21} = \frac{A_{1122}^H}{A_{1111}^H}.$$

Moreover, the homogenized Poisson's ratio  $\nu_{ij}$  are equally denoted *apparent Poisson's ratio* to highlight their reference to the homogenized unit cell. For example  $\nu_{12}$  characterizes the contraction of the structure in the direction of  $Oy$  axis when the cell stretched in the direction of  $Ox$  axis and in general  $\nu_{12} \neq \nu_{21}$ . However, if the microarchitecture of the unit

cell obeys cubic symmetry we have  $A_{1111}^H = A_{2222}^H$  and we trivially obtain that  $E_1 = E_2 = E^*$  and  $\nu_{12} = \nu_{21} = \nu^*$ .

**The optimization problem.** Next we discuss the framework of the optimization problem without presenting the details of the algorithm which is beyond the scope of the paper.

Let us assume that the unit cell  $Y$  is a working domain and consider  $\omega$  an open and bounded subset of  $Y$  representing the shape of the architected microstructure. The distance between the homogenized elastic moduli over the unit cell and target elastic moduli can be measured by the following cost functional,

$$J(\omega) = \frac{1}{2} \|\mathbb{A}^H(\omega) - \mathbb{A}^t\|_\eta^2$$

where  $\|\cdot\|_\eta$  is the weighted Euclidean norm,  $\mathbb{A}^t$  is the target elastic tensor, and  $\eta$  are the weight coefficients. We define a set of admissible shapes contained in the working domain  $Y$  and have a fixed volume by  $\mathcal{U}_{ad} = \{\omega \subset Y \text{ such that } |\omega| = V^t\}$ . Hence, the optimal shape design of the microarchitecture can be formulated as the following optimization problem:

$$\begin{aligned} & \inf_{\omega \subset \mathcal{U}_{ad}} J(\omega), \\ & \chi^{ml} \text{ satisfies (2.2)}. \end{aligned} \tag{2.3}$$

**Level set representation of the shape.** The shape  $\omega$  is represented in a fixed mesh inside the unit cell  $Y$  using the the level set method. If we denote by  $\phi$  a level set, then the corresponding shape  $\omega$  is defined in the following way:

$$\begin{cases} \phi(\mathbf{y}) = 0 & \text{if } \mathbf{y} \in \partial\omega \cap Y, \\ \phi(\mathbf{y}) > 0 & \text{if } \mathbf{y} \in Y \setminus \omega, \\ \phi(\mathbf{y}) < 0 & \text{if } \mathbf{y} \in \omega, \end{cases}$$

See also FIGURE 3 for a graphical example.

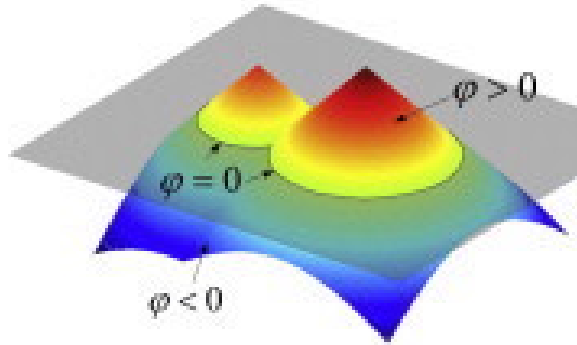


FIGURE 3. Schematic representation of the level set  $\phi$  of the domain  $\omega$

The optimization of  $J(\omega)$  is carried out by advecting an initial shape  $\omega_0$  with velocity  $v$  obtained from the shape derivative  $\langle J'(\omega) | \boldsymbol{\theta} \rangle$  in the direction  $\boldsymbol{\theta}$  (see Allaire, Jouve, Toader [4], Wang, Mei, Wang [35]). The advection is realized by solving the Hamilton-Jacobi equation,

$$\partial_t \phi + v |\nabla \phi| = 0,$$

where  $v$  is the velocity of the interface computed from the shape derivative  $\langle J'(\omega) \mid \boldsymbol{\theta} \rangle$ . The numerical algorithm can be summarized in the following steps:

- (i) Initialize the level set  $\phi^0$  corresponding to the initial form  $\omega_0$ .
- (ii) Update the level set  $\phi^0$  using the signed distance function  $d_{\omega_0}$ .
- (iii) Iterate until convergence for  $k \geq 0$ :
  - a. Calculate the local solutions  $\boldsymbol{w}_k^{m\ell}$  for  $m, \ell = 1, 2$  by solving the linear elasticity problem in  $Y$ .
  - b. Deform the domain  $\omega_k$  by solving the above Hamilton-Jacobi equation. The new shape  $\omega_{k+1}$  is characterized by the level set  $\psi^{k+1}$  after a time step  $\Delta t_k$ . The time step  $\Delta t_k$  is chosen so that  $J(\omega^{k+1}) \leq J(\omega^k)$ .
- (iv) If needed for stability reasons, re-initialize the level set functions  $\phi^k$ .

The complete algorithm as well as several examples are presented in Nika & Constantinescu [29]. The interested reader is encouraged to consult the works of Allaire [2], Allaire, Jouve & Toader [4], Allaire et. al. [5], Michailidis [26], Wang, Mei & Wang [35] for more details about the mathematical results and algorithmic issues for the solution method.

**Examples of optimal microstructures.** In all the examples that follow we have set the Young modulus for the void (or weak) material equal to  $E_0 = 0.0001$  and for the strong material to  $E_1 = 0.91$ . The Poisson's ratio for both phases was set to  $\nu = 0.3$ . The quadratic unit cell  $Y$  was meshed with a structured symmetric grid of  $100 \times 100$  quadrangular each formed of four equal triangular  $P1$  elements. All computations were carried out using an in house programming of the preceding algorithm [29] operating on **FreeFEM++** software [16].

We would like to remark that we only controlled the coefficients and is reported in Table 1 with varying values for the three different structures.

In all examples the target objective was defined only in terms of  $A_{1111}^H, A_{1122}^H, A_{2222}^H$ . The shear coefficient  $A_{1212}^H$  as well as the  $A_{1211}^H$  and  $A_{1222}^H$  coefficients were left free. Therefore only the elastic moduli of the unit cell corresponding to the direction 11 and 22 directions of strain and stresses were controlled. However all targets had as an underlying objective an apparent Poisson ratio which will be discussed next.

**Example 1.** The first microstructure to be optimized is a structure whose target apparent Poisson's ratio is equal  $\nu^* = -1.0$ . The volume constraint was set to  $V^t = 50\%$  and was enforced using a Lagrange multiplier computed by assuming that the optimality criterion was satisfied, namely  $\langle J'(\omega) \mid \boldsymbol{\theta} \rangle + \ell \langle V'(\omega) \mid \boldsymbol{\theta} \rangle = 0$ . The Lagrange multiplier was updated by imposing  $\ell^{n+1} = \frac{(\ell^n + \ell)}{2} + \epsilon(V - V^t)$ , where  $\epsilon$  is a small positive real number and  $\ell = -\langle J'(\omega) \mid \boldsymbol{\theta} \rangle / \langle V'(\omega) \mid \boldsymbol{\theta} \rangle$ . This technique has been initially proposed and discussed by Allaire and Pantz [6]. We further note that for this structure we enforced symmetry only along the  $Oy$  axis in the algorithm, by symmetrizing the shape after each iteration.

The initial and final shape of the microstructure on the unit-cell and as a periodic material are represented in figure 4. The final shape can be characterized as an inverted honeycomb structure and looks similar to the designs imagined by Almgren [8]. Its homogenized coefficients, displayed in Table 1, show that the structure exhibits orthotropic symmetry and a simple calculation yields  $\nu_{12} = -1.25$  and  $\nu_{21} = -0.42$ . Hence, the expansion of the structure along the  $Oy$  axis when stretched in the  $Ox$  axis is larger the expansion along the  $Ox$  axis when stretched in the  $Oy$  axis. This non-symmetric effect has been enabled as the symmetry relation was only imposed along the  $Oy$  axis in the algorithm.

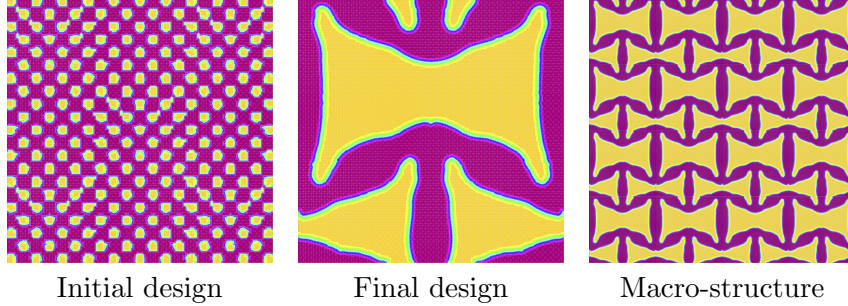


FIGURE 4. The design process of the material from initial guess to final macro-structure represented in the unit cell and as a periodic material. ● Young modulus of 0.91, ● void.

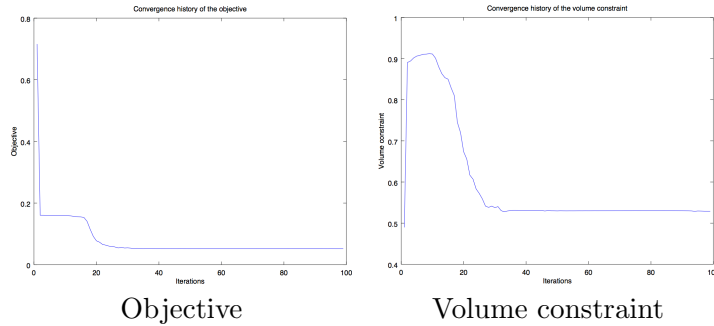


FIGURE 5. Convergence history of the objective function and the volume constraint.

The convergency history of the cost-functional and of the volume constraint displayed in FIGURE 5 shows that the target coefficient where reached in slightly more than 20 iteration and that the later iteration contributed only to small improvements without bringing the cost functional to less than 0.06 which corresponds to 92% decrease of the initial value. The gap with respect to the target moduli can be read from Table 1. It is interesting to remark, that the final optimized microstructure has a shear moduli close to 0. However the final apparent Poisson’s ratio is close to the imagined target as will be discussed in the comparison with the printed samples.

The volume constraint has a different evolution than the cost-functional with an initial increase given by the initial evolution of the holes and then a fast and a slow evolution which lies within the proposed range of the constraint.

**Example 2.** The second microstructure to be optimized is a structure whose target apparent Poisson’s ratio was also  $\nu^* = -1.0$ . The Young modulus and Poisson’s ratio are the same as in example 1. The volume constraint was of an inequality type, and was set to  $16\% \leq V^t \leq 60\%$ . For the enforcement of the constraint we used an augmented Lagrangian. The Lagrange multipliers for the weight were updated the following way,  $\ell^{n+1} = \ell^n + \beta(V - V^t)$ , where  $\beta$  is a penalty term that was updated every 10 iterations. We point out that the augmented Lagrangian approach would require a re-computation of the shape derivative. As result, initial guesses for  $\ell$  and  $\beta$  would both have an effect on final optimal shape (see also the discussion on the algorithmic issues in Nika & Constantinescu [29]).



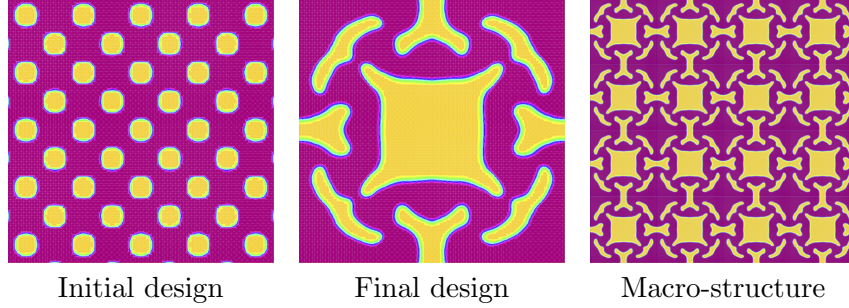


FIGURE 6. The design process of the material from initial guess to final macro-structure represented in the unit cell and as a periodic material. ● Young modulus of 0.91, ● void.

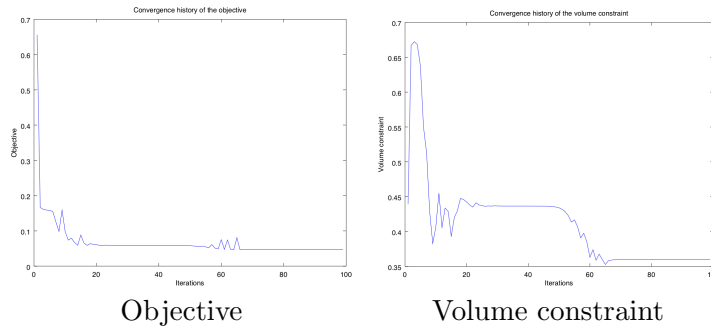


FIGURE 7. Convergence history of the objective function and the volume constraint.

Let us further specify, that we enforced in the symmetry of the shape along both the  $Ox$  axis and  $Oy$  axis, by symmetrizing the shape during the algorithmic iterations. The resulting structure exhibits cubic symmetry with apparent Poisson's ratio  $\nu^* = \nu_{12} = \nu_{21} = -0.42$ . Hence, the expansion along the  $Ox$  and  $Oy$  axis is the same. As in the first example, one can read the target and final elastic moduli from Table 1. As before, the final optimized microstructure has a shear moduli close to 0 and the final apparent Poisson ratio is close to the imagined target.

The evolution of the cost-functional displayed in Figure 7 shows that the decrease was not monotonous and that several interventions in the step size and algorithmic details were necessary to reestablish convergence. Moreover these moments are correlated with the important variations in the volume constraint, however the final volume ratio at approximately 35% lies in the middle of the imposed interval.

**Example 3.** The third microstructure to be optimized is a structure whose target apparent Poisson's ratio is  $\nu^* = -0.5$ . The volume constraint is set to  $V^t = 40\%$  and is updated the same exact way as in the first example. Again, as in example 2, we symmetrized the structure along the  $Ox$  and  $Oy$  axis.

The structure exhibits cubic symmetry with apparent Poisson ratio  $\nu^* = -0.47$ . Moreover one can remark that the final elastic moduli are very close to the target and that this structure has a shear moduli which is of the same order of magnitude as the other moduli.

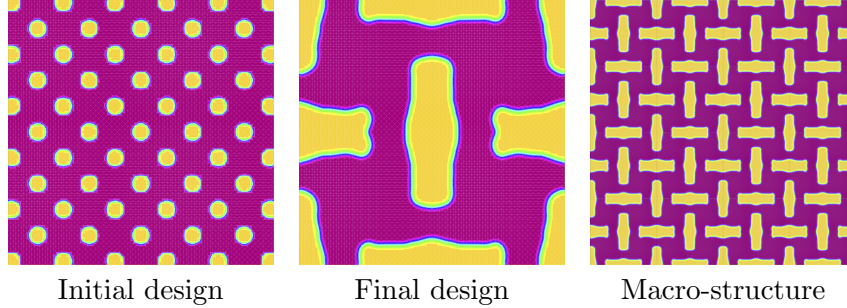


FIGURE 8. The design process of the material from initial guess to final macro-structure. ● Young modulus of 0.91, ● void.

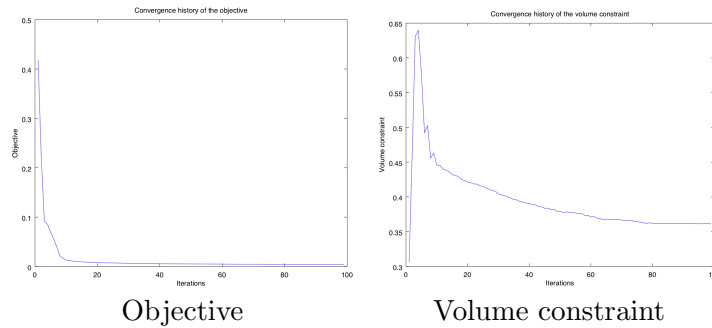


FIGURE 9. Convergence history of objective function and the volume constraints.

### 3. ANALYSIS OF FABRICATED POLYMER STRUCTURES

**Manufacturing process: equipment and materials.** The optimal shapes have been additively manufactured with digital light processing stereo-lithography technology (DLP) using a EMBER DLP 3D printer. A digital projector screen flashes a single image of each layer across the entire surface of the vat filled of photo-sensitive liquid resin at once, causing chains of molecules to link and thus forming solid polymer. The process is repeated until the 3D model is complete. Then the vat is drained of liquid, revealing the solidified model and the solid model is washed with a solvent.

The printer has a resolution of  $50\ \mu\text{m}$ , corresponding to 1 pixel in the digital projector screen, and a range of the processing layer thickness of  $10 - 100\ \mu\text{m}$ . The largest processing build volume is  $64\ \text{mm} \times 40\ \text{mm} \times 134\ \text{mm}$  (note that  $64\ \text{mm} \times 40\ \text{mm}$  correspond to a  $1280 \times 800$  pixels picture). For a thickness of  $25\ \mu\text{m}$  per layer, the speed range is of  $18\ \text{mm}/\text{h}$ . The printable minimal feature size of the specimens is announced at  $0.4\ \text{mm}$  corresponding roughly to 8 pixels.

We selected a rubber-like material, commercially denoted as GM08b, as the base material because of its compliant nature. Figure 10 displays a representative tensile stress–strain curve of the GM08b material. As expected for a rubber-like material it does not display an ideal linear elastic behavior, it exhibits a gradually variation of the stiffness with increasing strain. However, we can linearly approximate the stiffness with a  $7\ \text{MPa}$  Young’s modulus in accordance with one of the manufacturers data sheet (see <https://dl.airtable.com>).

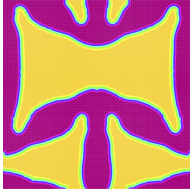
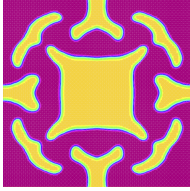
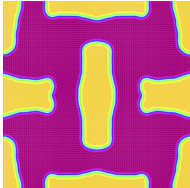
Target tensor $\mathbb{A}^t$	Homogenised tensor $\mathbb{A}^H$	Unit cell
$\begin{pmatrix} 0.1 & -0.1 & 0 \\ -0.1 & 0.1 & 0 \\ 0 & 0 & G \end{pmatrix}$	$\begin{pmatrix} 0.12 & -0.05 & 0 \\ -0.05 & 0.04 & 0 \\ 0 & 0 & 6 \times 10^{-3} \end{pmatrix}$	
$\begin{pmatrix} 0.1 & -0.1 & 0 \\ -0.1 & 0.1 & 0 \\ 0 & 0 & G \end{pmatrix}$	$\begin{pmatrix} 0.12 & -0.05 & 0 \\ -0.05 & 0.12 & 0 \\ 0 & 0 & 0.003 \end{pmatrix}$	
$\begin{pmatrix} 0.2 & -0.1 & 0 \\ -0.1 & 0.2 & 0 \\ 0 & 0 & G \end{pmatrix}$	$\begin{pmatrix} 0.19 & -0.09 & 0 \\ -0.09 & 0.19 & 0 \\ 0 & 0 & 0.6 \end{pmatrix}$	

TABLE 1. Target tensor values and homogenized tensor values computed numerically for each corresponding shape.

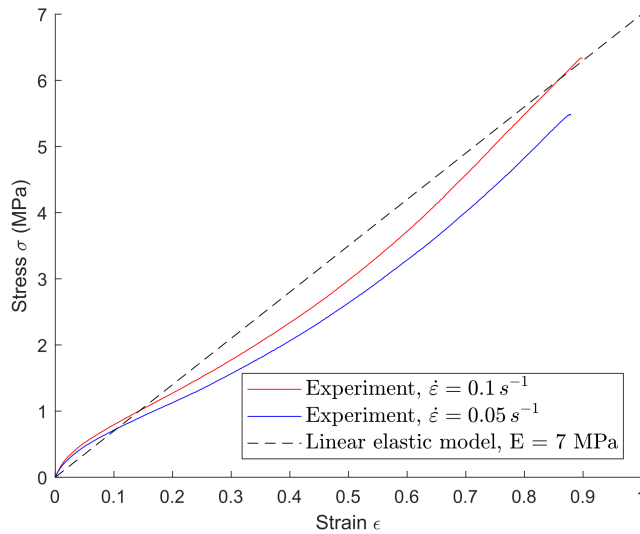


FIGURE 10. Uniaxial tensile test. Homogeneous stress-strain curves

Moreover, let us further remark that the Poisson coefficient of the material has not been measured, but we should expect it to be close to the incompressible limit of  $\nu \approx 0.5$ .

The optimal shapes obtained in examples 1–3 (see FIGURE 4, FIGURE 6, FIGURE 8) are represented by the final level set function. The later presents a smooth variation between values corresponding to the two materials in a neighborhood of their interface and therefore

the levelset representation has been binarized and then extruded in the  $Oz$  direction in order to create a 3D object. More precisely, the 3D-printed samples have been produced by the following procedure:

- (i) *Binarize the level set function representing by shape optimisation. As the later presents a smooth variation between values corresponding to the two materials in a neighborhood of their interface.*
- (ii) *Create a periodic array for each sample:  $8 \times 6$  unit cells for example 1,  $5 \times 4$  unit cells for example 2 and example 3, using the software ImageJ [31]. The final result was a binarised  $1280 \times 800$  pixels image (see Figure 11 for details) .*
- (iii) *Extrude the preceding image to obtain the 3D sheet of the desired height. The final dimensions of the printed samples are  $64 \times 38 \times 6$  mm for example 1 and  $64 \times 40 \times 6$  mm for example 2 and 3.*
- (iv) *Print the files with the following processing parameters: laser power was 5W, the exposure time 1 s per layer and the layer thickness was  $50 \mu\text{m}$ .*
- (v) *Wash the samples in an isopropanol bath for 5 min*
- (vi) *Post-cure the samples for 30 min in an UV oven at 2000W.*

#### 4. TESTING AND FULL-FIELD DISPLACEMENT MEASUREMENT USING DIGITAL IMAGE CORRELATION

A series of uniaxial static tensile tests were undertaken to assess the tensile properties of the auxetic lattice structures by using a home-made testing machine with a symmetric displacement of the two crossheads and equipped with a 100 N load cell. The tensile tests were performed at a rate of  $0.05 \text{ mm/s}$  up to  $3 \text{ mm}$ , which corresponds to a strain rate of  $\dot{\varepsilon} = 10^{-3} \text{ s}^{-1}$  up to a maximal strain of  $\varepsilon = 5\%$ .

Several pictures were taken during the tensile experiment and the complete displacement field of the specimen was computed using digital image correlation (DIC). The pictures with a resolution of  $4904 \times 3280$  were obtained using a high-resolution digital camera (Schneider Optics 8-bit camera with a Makro-UNIFOC 100/77 lens) mounted on the tensile testing machine and grey scale pictures were recorded every second during the loading. The camera is mounted on a perpendicular axes with respect to the plane of the specimen, which enables the direct use of a 2D DIC. To improve the precision of the measurement, a white speckle pattern was placed on the sample by airbrushing.

The DIC was done using the CorrelManuV 2D (CMV) software, developed by M. Bornert [7]. The processed displacement field corresponds to a single unit cell in the middle of the structure at 5 different loading time steps, using a  $100 \times 100$  grid, i.e. having 10000 measurement points. For each node, the subset size was set to  $20 \times 20$  pixels, while the searching area was set to  $100 \times 100$  pixels. The measurement included a computation without transformation, i.e. rotation of the subset window and a re-optimisation allowing transformations with a reduced searching area of  $30 \times 30$  pixels.

**Finite Element Computations.** A series of finite element computation were undertaken under the assumption small strains, large displacements and plane stress using the finite element solver Cast3M2018 (<http://www-cast3m.cea.fr>). The mesh was obtained using image processing from the binarized images of the optimal level set function and completed to the sample geometry including the grips. The sample was loaded by the

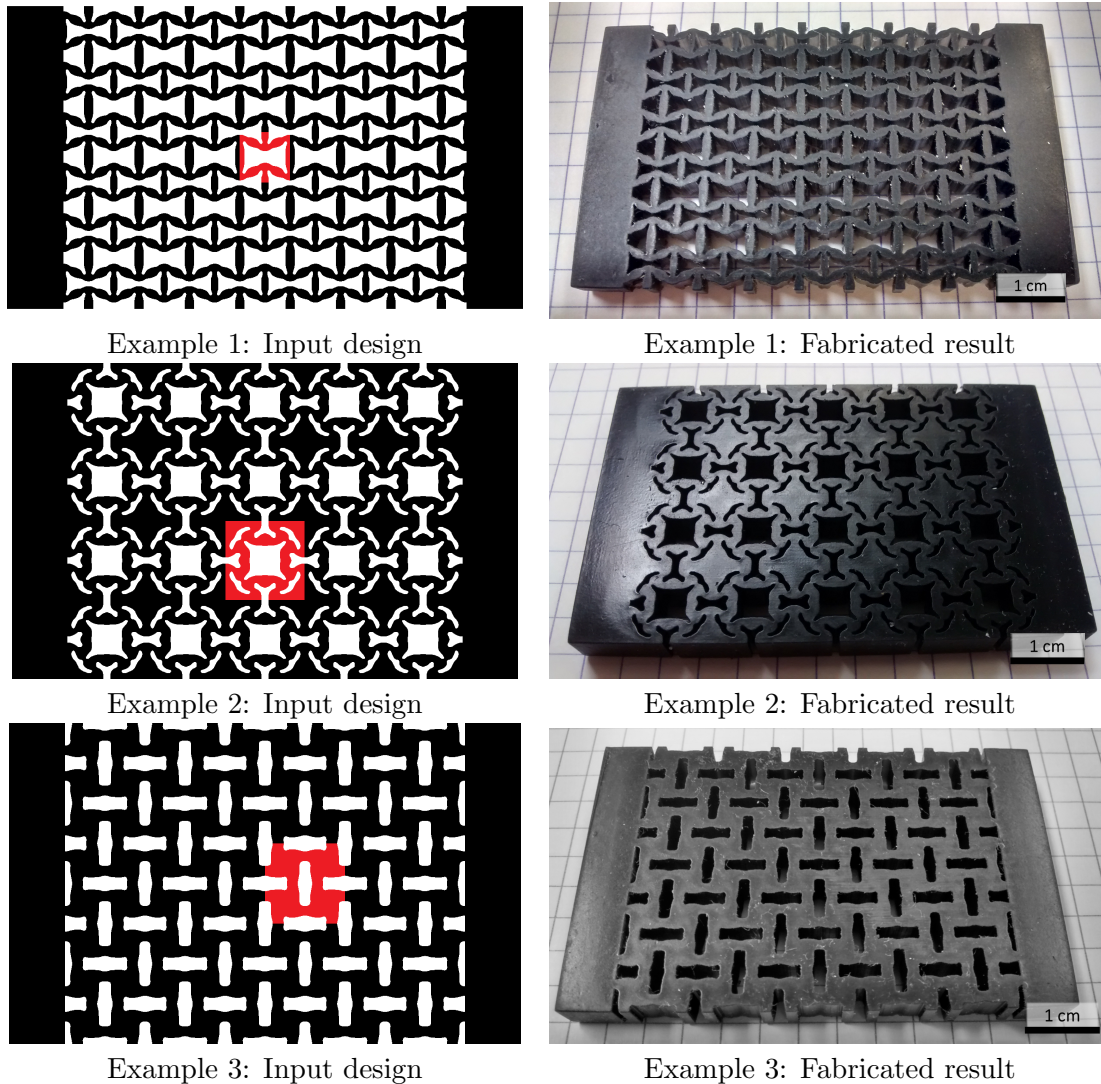


FIGURE 11. Fabricated auxetic microstructures with different apparent Poisson ratios (right) and the initial input design (left).

imposing the displacements of the clamps of the tensile machine. Other boundaries were stress free edges. The elastic behavior was considered to be linear and corresponded to the linear approximation of the base material displayed in FIGURE 12.

**Results.** The stress strain response under a uniaxial tensile test for the three materials are displayed in FIGURE 12. One can easily observe a linear behavior of the samples that up to a maximal strain of 5% strain despite the nonlinearity of the rubber-like base material in the same strain range. This indicates that the samples have as expected structural deformation where different parts of the "lattice" behave as rigid struts and deformable hinges. This effect will be highlighted by the DIC measurements discussed later.

Furthermore, one can directly observe a lateral expansion during the tensile extension indicating a negative apparent Poisson's ratio for all the samples. The precise measurements of the apparent Poisson's ratio corresponding to a single central unit cell are presented in

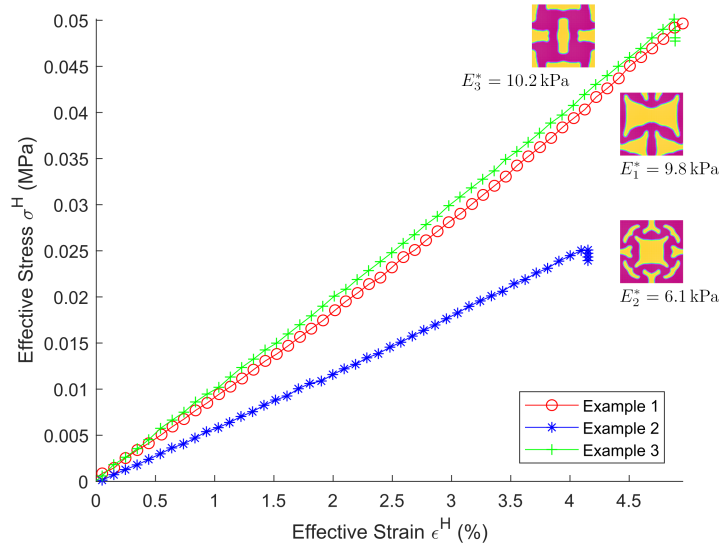


FIGURE 12. Stress strain curves for all three examples obtained by performing a uniaxial tensile test. All three materials exhibit linear behaviour for strains up to 5%.

FIGURE 16. The precise method for the computation of the apparent Poisson’s ratio of a single unit cell from DIC measurements was based on homogenization assumptions and is presented in detail in the appendix A. The results show that the initial apparent Poisson ratio was for all samples close to the target value used in the optimization process and was not degraded during the manufacturing process. During tensile loading, the apparent Poisson’s ratio tends to increase, indicating a decrease of the “auxeticity” of the samples of up to increases by 10% for a 5% strain. Let us first remark, that the evolution is close to predictions of the deformation of the samples obtained by the finite element method under the assumption of large displacements. Second, one can remark that the evolution of the apparent Poisson ratio with applied strain has already been observed and discussed in [14] on polymeric filament structure. Moreover, they arrived to correct the phenomenon up to 20% strain using a nonlinear material behavior in the optimization process, see [14, 37] for more details on the subject. In the case of the optimization procedure presented here, the extension to nonlinear material behavior is currently under works.

The displacements fields obtained using DIC permit a further comparison with predictions and give an insight of the deformation mechanism in the samples, i.e. how the structure moves and deforms. FIGURES 13–15 display the measured and the computed vertical displacement, i.e. the  $u_y$  displacement component, of the central unit-cell. A comparison of the values and the shapes of the colormaps exhibits a good match between the measurements and finite element prediction. Moreover the displacement fields permits to better understand the local movements of the microstructure which conducts to the global auxeticity effect by combining almost rigid regions submitted to translations and rotations with local concentrated deformation exhibiting local hinges.

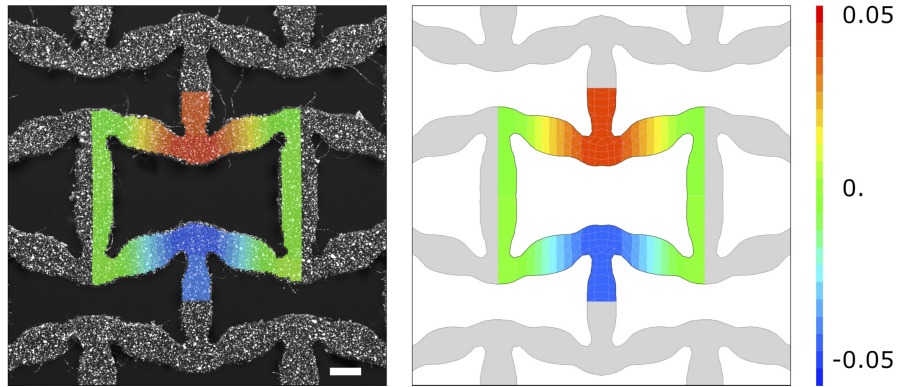


FIGURE 13. Dimensionless values of the vertical displacement field for the unit cell of the structure in example 1 as measured using Digital Image Correlation (right) and Finite Element Analysis (left). Scale bar is 1 mm.

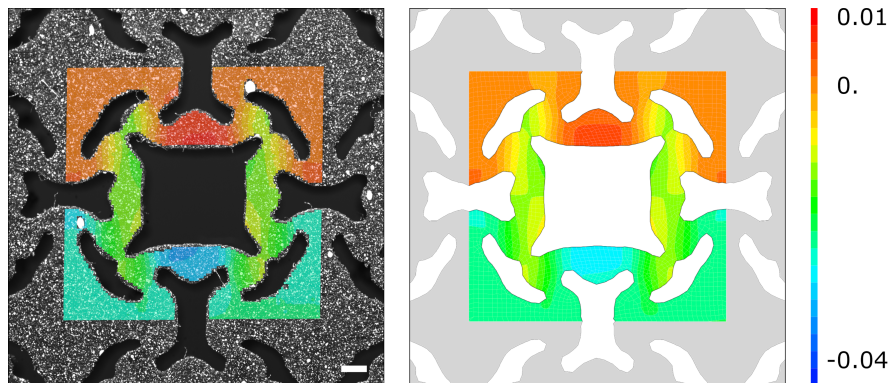


FIGURE 14. Dimensionless values of the vertical displacement field for the unit cell of the structure in example 1 as measured using Digital Image Correlation (left) and Finite Element Analysis (right).

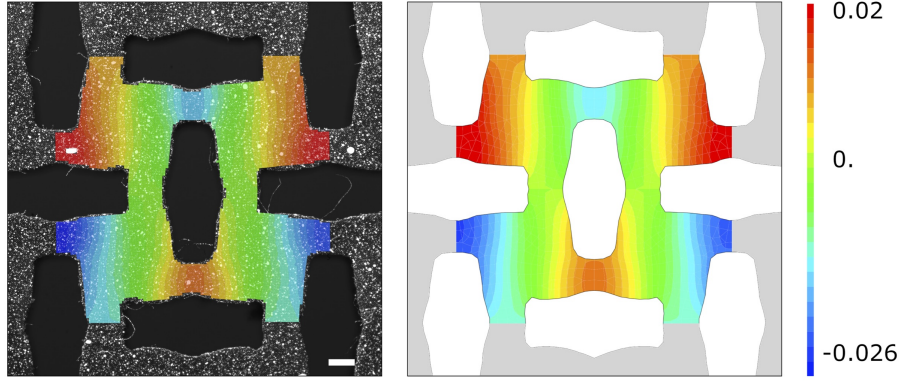


FIGURE 15. Dimensionless values of the vertical displacement field for the unit cell of the structure in example 3 as measured using Digital Image Correlation (left) and Finite Element Analysis (right).

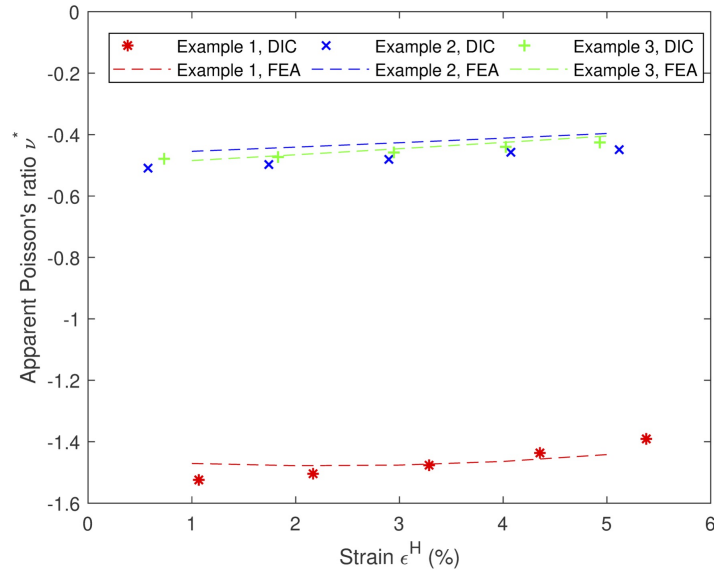


FIGURE 16. Evolution of the apparent Poisson's ratio plotted as a function of the strain. We observe the all three materials lose their auxeticity as the uniaxial strain increases.

## 5. CONCLUSION

This paper presented a complete design cycle for auxetic materials based on a topology optimization of the microstructure, the manufacturing of the material with a periodic microstructure using a commercial stereolithography printer and its testing. The topology optimization technique was based on the level set method and the Hadamard shape derivative to track the topological changes imposed by the variation of the cost functional.



The results showed that optimal shapes could be directly printed without additional enhancement of the surface, which is a direct consequence of the in the smoothed interface technique used in the optimization. Moreover the manufactured materials had the designed mechanical behavior. The targeted apparent Poisson's ratios have been experimentally attained and the local material behavior was close to predictions obtained by the finite element method. However, the results showed that the nonlinear material behavior both in terms of the constitutive law and of large strains and displacements should be included in the design process in order to control the target materials in the large strains regime.

The topology optimization process proved to be efficient tool to reach the desired apparent Poisson's ratios. However, the process was not as efficient in reaching a precise tensor of elastic moduli. The theoretical problem of reachable elasticity tensors has theoretically been solved using laminates in the seminal paper of Milton & Cherkaev [27] starting from two isotropic materials with arbitrary Young moduli. Given geometric and materials constraints that 3D printing introduces we are not certain that all targets of elastic moduli can be attained. In other words, the definition of the set of elastic moduli determined by all printable designs is a priori not know. Moreover, we are in need of a simple method to assess the set of realizable tensors when starting from a combination of real materials and given geometry constraints imposed by the 3D printer constraints.

The designed examples had two or three non-zero eigenelastic moduli and indicate that the design of unimode, bimode, pentamode, etc. materials as theoretically proposed in [27] could be pursued by topology optimization.

#### ACKNOWLEDGMENTS

This work is financed by the french-swiss ANR-SNF project MechNanoTruss (ANR-15-CE29-0024-01). AC and GN would like to express their gratitude to Chiara Daraio for fruitful discussion on the design of lattice structures and to Gregoire Allaire and Georgios Michailidis for lending their expertise on the numerical and algorithmic issues of the optimization.

#### REFERENCES

1. G. Allaire, *Shape Optimization by the Homogenization Methods*, Springer Verlag, (2001).
2. G. Allaire, *Conception optimale de structures*, Collection Mathématiques et Applications. Springer (2006).
3. G. Allaire, E. Bonnetier, G. Francfort, F. Jouve, *Shape optimization by the homogenization method*, Numerische Mathematik 76 (1997) pp. 2768.
4. G. Allaire, F. Jouve, A.-M. Toader, *Structural optimization using sensitivity analysis and a level set method*, J Comp Phys, 194/1 (2004), pp. 363-393.
5. G. Allaire, C. Dapogny, G. Delgado, G. Michailidis, *Multi-phase structural optimization via a level set method*. ESAIM: Control, Optimisation and Calculus of Variations, 20(2), (2014), pp. 576-611.
6. G. Allaire, O. Pantz, *Structural optimization with FreeFem++*. Struct Multidisc Optim 32 (2006) pp. 173-181.
7. L. Allais, M. Bornert, T. Bretheau, D. Caldemaison, *Experimental characterization of the local strain field in a heterogeneous elastoplastic material*, Acta Metallurgica et materialia 42 (11), (1994) pp. 3865-3880.
8. F. Almgren *An isotropic three dimensional structure with Poisson's ratio = -1*, J. of Elasticity, **15** (1985) pp. 427-430.
9. N. Bakhvalov, G. Panasenko, *Homogenisation: averaging processes in periodic media: mathematical problems in the mechanics of composite materials*, Kluwer Academic Publishers (1989).

10. M. Bendsoe, N. Kikuchi, *Generating optimal topologies in structural design using a homogenization method*, Comput Methods in Applied Mech Eng 71 (1988) pp. 197224.
11. M. Bendsoe, O. Sigmund, *Topology optimization: theory, methods and applications*, Springer, (2004).
12. O. Bilal, R. Susstrunk, C. Daraio, S. Huber, *Intrinsically polar elastic metamaterials*, Adv. Mater. 29 (2017) 1700540.
13. D. Cioranescu, P. Donato, *Introduction to Homogenization*, Oxford Lecture Series in Math. Appl., 17, Oxford University Press (1999).
14. A. Clausen, F. Wang and J S Jensen, O. Sigmund and J A Lewis, *Topology optimized architectures with programmable Poisson's ratio over large deformations*, Advanced Materials (2015) pp. 5523–5527
15. C.S. Ha, R.S. Lakes, M.E. Plesha *Design, fabrication, and analysis of lattice exhibiting energy absorption via snap-through behavior*. Materials & Design 141 (2018), pp. 426–437.
16. F. Hecht, *New development in FreeFem++*. J. Numer. Math. 20 (2012), no. 3-4, 251265. 65Y15
17. S. Hou, T. Liu, Z. Zhang, X. Han, Q. Li *How does negative Poisson's ratio of foams filler affect crash-worthiness?*. Materials & Design 82 (2015), pp. 247–259.
18. G. Imbalzano, P. Tran, T. D. Ngo, P. V. S. Lee, *A numerical study of auxetic composite panels under blast loadings*, Composite Structures, **135**, (2016) pp. 339–352.
19. C. Korner, Y. Liebold-Ribiero, *A systematic approach to identify cellular auxetic materials*, Smart Mater. Struct., **24**, (2015) pp. 339–352.
20. R. S. Lakes, *Foam structures with negative Poisson's ratio*, Science 235 (1987) pp. 1038–1040.
21. R. S. Lakes, *Advances in negative Poisson's ratio materials*, Adv. Mater. **5** (1993) pp. 293–296.
22. R. S. Lakes, *Elastic freedom in cellular solids and composite materials*, in Mathematics of Multiscale Materials, K. Golden, G. Grimmert, R. James, G. Milton, P. Sen, IMA vol. 99, Springer, NY, Berlin, (1998), pp. 129–153.
23. R.S. Lakes, K. Elms, *Indentability of conventional and negative Poisson's ratio foams*, J Compos Mater **27**(12) (1993) pp. 1193–1202.
24. T. Li, Y. Chen, X. Hu, Y. Li, L. Wang, *Exploiting negative Poisson's ratio to design 3D-printed composites with enhanced mechanical properties*, Materials & Design 142 (2018) pp. 247–258.
25. C.C. Mei, B. Vernescu, *Homogenization methods for multiscale mechanics*, Singapore: World-Scientific Publishing (2010).
26. G. Michailidis, *Manufacturing Constraints and Multi-Phase Shape and Topology Optimization via a Level-Set Method*, PhD thesis at Ecole Polytechnique X, (2014).
27. G. Milton, A. Cherkaev, *Which elasticity tensors are realizable?*, J. Eng. Mater. Technol 117(4), (1995) pp. 483-493.
28. F. Murat, J. Simon, *Etudes de problmes doptimal design*, Lectures Notes in Computer Science 41, Springer Verlag, Berlin, (1976) pp. 54-62.
29. G. Nika, A. Constantinescu, *Design of multi-layer material using inverse homogenization and a level set method* (submitted).
30. S. Osher, J. Sethian, *Fronts propagating with curvature dependent speed: algorithms based on hamilton-jacobi formulations*, J Comput Phys 79 (1988) pp. 1249.
31. Rueden, Curtis T and Schindelin, Johannes and Hiner, Mark C and DeZonia, Barry E and Walter, Alison E and Arena, Ellen T and Eliceiri, Kevin W, *ImageJ2: ImageJ for the next generation of scientific image data*, BMC bioinformatics (2017) pp. 529.
32. E. Sanchez-Palencia, *Non-homogeneous media and vibration theory*, Lecture Notes in Physics, Springer-Verlag, (1980).
33. E. Sanchez-Palencia, A. Zaoui (eds) *Homogenization techniques for composite media*, Lecture Notes in Physics, Springer-Verlag, (1987).
34. Schumacher, C., Bickel, B., Rys, J., Marschner, S., Daraio, C., Gross, M.H. *Microstructures to control elasticity in 3D printing*. ACM Trans. Graph., 34, 136:1-136:13.
35. X. Wang, Y. Mei, M.Y. Wang *Level-set method for design of multi-phase elastic and thermoelastic materials*, Int J Mech Mater Des 1 (2004) pp. 213239.
36. M.Y. Wang, X. Wang, *“Color” level sets: A multiple multi-phase method for structural topology optimization with multiple materials*, Comp Meth App Mech Eng 193(6) (2004) pp. 469496.

## APPENDIX A. COMPUTATION OF THE APPARENT POISSON'S RATIO

This appendix reviews the mathematical approach that was used to measure/compute the apparent Poisson's ratio of a unit cell in both measurement by digital image correlation and numerical estimation using a finite element method. For the following computation, we place ourselves in the case of small strain assumption.

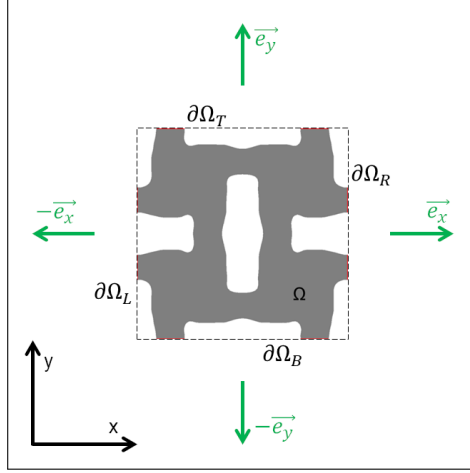


FIGURE 17. Representation of a unit cell

The effective material is supposed to carry a natural orthotropic material behaviour. The apparent Poisson's ratio  $\nu_{12}$ , characterising the transverse strain of the structure in the direction Oy axis when stretched in the direction Ox, is defined as:

$$\nu_{12}^* = \frac{A_{1122}^H}{A_{2222}^H} \quad (\text{A.1})$$

We remind that  $A_{1122}^H$  and  $A_{2222}^H$  are coefficients of the effective elastic stiffness tensor. In general  $\nu_{12} \neq \nu_{21}$ . During a uniaxial tensile test in the direction Ox, equation (A.1) yields to the negative of the ratio of macroscopic transverse strain to macroscopic axial strain:

$$\nu_{12}^* = -\frac{\varepsilon_{22}^H}{\varepsilon_{11}^H} \quad (\text{A.2})$$

In small strain assumption, the strain field can be linearised as:

$$\boldsymbol{\varepsilon}^H = \langle \boldsymbol{\varepsilon} \rangle_{\Omega} = \frac{1}{2} \left( \langle \mathbb{F} \rangle_{\Omega}^T + \langle \mathbb{F} \rangle_{\Omega} \right) - \mathbb{I} \quad (\text{A.3})$$

where  $\mathbb{F}$  is the average transformation gradient. Considering the small strain assumption:

$$\langle \mathbb{F} \rangle_{\Omega} = \frac{1}{V_{\Omega}} \int_{\Omega} (\mathbb{I} + \nabla \mathbf{u}) d\Omega \quad (\text{A.4})$$

Using Ostrogradsky's theorem, we can express the transformation gradient at the boundary  $\partial\Omega$ :

$$\langle \mathbb{F} \rangle_{\Omega} = \frac{1}{V_{\Omega}} \left( \int_{\Omega} \mathbb{I} d\Omega + \oint_{\Gamma} \mathbf{u} \otimes \mathbf{n} d\Gamma \right) \quad (\text{A.5})$$

Study of a unit cell

$$\langle \mathbb{F} \rangle_{\Omega} = \mathbb{I} + \frac{1}{V_{\Omega}} \left( \int_{\partial\Omega_T} \mathbf{u} \otimes \mathbf{e}_y d\Gamma + \int_{\partial\Omega_B} \mathbf{u} \otimes (-\mathbf{e}_y) d\Gamma + \int_{\partial\Omega_R} \mathbf{u} \otimes \mathbf{e}_x d\Gamma + \int_{\partial\Omega_L} \mathbf{u} \otimes (-\mathbf{e}_x) d\Gamma \right) \quad (\text{A.6})$$

$$\langle \mathbb{F} \rangle_{\Omega} = \mathbb{I} + \frac{1}{V_{\Omega}} \begin{bmatrix} \int_{\partial\Omega_R} u_x d\Gamma - \int_{\partial\Omega_L} u_x d\Gamma & \int_{\partial\Omega_T} u_x d\Gamma - \int_{\partial\Omega_B} u_x d\Gamma \\ \int_{\partial\Omega_R} u_y d\Gamma - \int_{\partial\Omega_L} u_y d\Gamma & \int_{\partial\Omega_T} u_y d\Gamma - \int_{\partial\Omega_B} u_y d\Gamma \end{bmatrix} \quad (\text{A.7})$$

Thus from equation (A.3):

$$\begin{cases} \varepsilon_{11} = \frac{1}{V_{\Omega}} \left( \int_{\partial\Omega_R} u_x d\Gamma - \int_{\partial\Omega_L} u_x d\Gamma \right) \\ \varepsilon_{22} = \frac{1}{V_{\Omega}} \left( \int_{\partial\Omega_T} u_y d\Gamma - \int_{\partial\Omega_B} u_y d\Gamma \right) \end{cases} \quad (\text{A.8})$$

For each edge of the square unit cell, the integral of the contour is computed by integrating the displacement of the material in contact with the edge. In other words, the void phase is not considered in the computation.

$$\nu_{12}^* = - \frac{\int_{\partial\Omega_T} u_y d\Gamma - \int_{\partial\Omega_B} u_y d\Gamma}{\int_{\partial\Omega_R} u_x d\Gamma - \int_{\partial\Omega_L} u_x d\Gamma} \quad (\text{A.9})$$

In practice, using a finite element method, equation (A.9) becomes :

$$\nu_{12}^* = - \frac{\frac{1}{N_T} \sum_{i=1}^{N_T} u_y^i - \frac{1}{N_B} \sum_b^{N_B} u_y^i}{\frac{1}{N_R} \sum_{i=1}^{N_R} u_x^i - \frac{1}{N_L} \sum_{i=1}^{N_L} u_x^i} \quad (\text{A.10})$$

where  $N_i, i \in \{T, B, R, L\}$  are respectively the number of nodes on top, bottom, right and left edges.

LMS, CNRS, ÉCOLE POLYTECHNIQUE, UNIVERSITÉ PARIS-SACLAY, 91128 PALAISEAU, FRANCE.  
*E-mail address:* [filippo-matteo.agnelli@polytechnique.edu](mailto:filippo-matteo.agnelli@polytechnique.edu)

LMS, CNRS, ÉCOLE POLYTECHNIQUE, UNIVERSITÉ PARIS-SACLAY, 91128 PALAISEAU, FRANCE.  
*E-mail address:* [andrei.constantinescu@polytechnique.edu](mailto:andrei.constantinescu@polytechnique.edu)

LMS, CNRS, ÉCOLE POLYTECHNIQUE, UNIVERSITÉ PARIS-SACLAY, 91128 PALAISEAU, FRANCE.  
*E-mail address:* [grigor.nika@polytechnique.edu](mailto:grigor.nika@polytechnique.edu)